Materials & Design 210 (2021) 110084

Contents lists available at ScienceDirect

Materials & Design

journal homepage: www.elsevier.com/locate/matdes

Fatigue crack nucleation and growth in laser powder bed fusion AlSi10Mg under as built and post-treated conditions

Juan Guillermo Santos Macías [a,*], Chola Elangeswaran [b], Lv Zhao [a,c,d], Jean-Yves Buffière [e], Brecht Van Hooreweder [b], Aude Simar [a]

[a] Université catholique de Louvain, Institute of Mechanics, Materials and Civil Engineering, IMAP, B-1348 Louvain la Neuve, Belgium
[b] KU Leuven, Department of Mechanical Engineering, B-3001 Leuven, Belgium
[c] Huazhong University of Science and Technology, School of Aerospace Engineering, Department of Mechanics, Wuhan, China
[d] Hubei Key Laboratory of Engineering Structural Analysis and Safety Assessment, Wuhan, China
[e] INSA Lyon, MATEIS, F-69621 Villeurbanne, France

HIGHLIGHTS

- LPBF AlSi10Mg presents early fatigue crack nucleation due to the presence of porosity.
- FSP reduces porosity and improves fatigue life, delaying fatigue crack nucleation.
- Both 300°C for 2h and FSP induce ductilisation, reducing fatigue crack growth rate.

GRAPHICAL ABSTRACT

Friction stir processing improves both fatigue life in general and fatigue crack growth rate in particular due to its porosity reduction effect, not achieved by SRHT, delaying crack nucleation, and its marked impact on ductility.

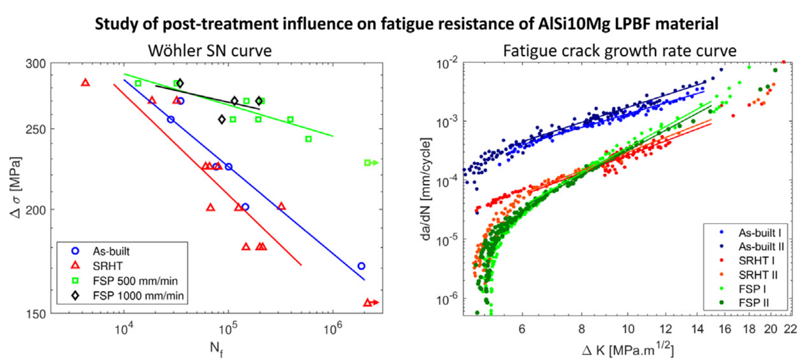

ARTICLE INFO

Article history:
Received 7 June 2021
Revised 9 August 2021
Accepted 2 September 2021
Available online 02 September 2021

Keywords:
Laser powder bed fusion
Friction stir processing
Stress relieve heat treatment
AlSi10Mg
Total fatigue life
Fatigue crack growth

ABSTRACT

Numerous efforts have been devoted to produce reliable additive manufactured (AM) materials for structural applications. However, the critical fatigue issue poses a significant hurdle in relation to the nature of this production method. Despite the relative flexibility of the laser powder bed fusion (LPBF) AM process, there exists a limitation in the possibility of tailoring parameters to obtain a satisfactory combination of porosity and surface roughness for adequate fatigue resistance. This quandary arises interest for post-treatments that could help overcome this limitation. Friction stir processing was proved to be a viable solution to improve fatigue behaviour of LPBF AlSi10Mg in the present work. Indeed, thanks to this post-process that reduces overall porosity and eliminates critical defects while keeping a satisfactory fine microstructure and static mechanical behaviour, fatigue resistance of the material was significantly enhanced. In contrast, the other studied post-process, stress relieve heat treatment, did not reduce porosity, which remained the main factor behind fatigue crack nucleation, cyclic life of the material being thus little affected with respect to the as built state. Furthermore, both post-treatments decreased fatigue

* Corresponding author.
E-mail address: juan.santos@uclouvain.be (J.G. Santos Macías).

https://doi.org/10.1016/j.matdes.2021.110084
0264-1275/

crack growth rate by an order of magnitude. This is interpreted as being due to plasticity induced crack closure and crack branching.

1. Introduction

Fatigue resistance is a very important aspect in parts subjected to mechanical loads since failure under cyclic loading, occurring at a lower stress than under static forces, is often a more critical and limiting factor [1,2]. In the case of transport applications, where the presence of dynamic loads is ubiquitous, fatigue life plays a central role in part design.

Additive manufacturing (AM) is gaining momentum as a key tool to help in the development of more optimal parts in various fields [3]. In structural applications AM represents a valuable contribution stemming from design flexibility [4]. Metal AM can also give rise to the creation of lighter structural parts in the transport industry, especially in the aerospace field. Aluminium-based AM alloys are particularly suitable for this purpose, laser powder bed fusion (LPBF) and AlSi10Mg being a popular process-material couple [5].

LPBF AlSi10Mg presents good static mechanical behaviour with relatively low density. The rapid solidification characteristic of the AM process results in a very fine microstructure and significantly high strength, which, coupled to the design flexibility advantage, should make this alloy a good candidate for lightweight structural applications [6]. The as built (AB) material has however a limited ductility, but, more importantly, the fatigue resistance is compromised by a defect characteristic to the AM process, porosity [6–10]. This remains the main shortcoming hindering a better fatigue life, ahead of anisotropy or residual stress influences [5,11–14].

Different solutions have been explored to improve fatigue resistance of LPBF AlSi10Mg, ranging from parameter optimisation [15,16] to post-treatments. The typical heat treatments applied to this alloy are the stress relieve heat treatment (SRHT) and the T6 treatment [17]. SRHT is usually performed at 270–300 °C for 90–120 min [18,19]. The reduction in residual stresses can have an impact on the fatigue behaviour of a certain part, but this does not imply a positive influence of heat treatments on the fatigue resistance from the material viewpoint [14,20–22]. Other possibilities can be the hot isostatic pressing (HIP) or friction stir processing (FSP) thermomechanical treatments. HIP is performed in a dedicated oven, where heat and pressure are applied simultaneously to the manufactured part. Unfortunately this post-process has not produced satisfactory results on AM aluminium alloys so far [14,22–25]. FSP, derived from friction stir welding (FSW), consists on traversing the area of interest of the part to be treated with a non-consumable, rotating cylindrical tool, composed of a shoulder with a pin at the end [26]. FSP has shown more potential for overall mechanical behaviour improvement [7,23,27,28].

From a practical standpoint, FSP is a very promising approach to improve mechanical behaviour [7,23,27,28] because it can be applied locally and at surface level (see Fig. 1), at the precise location where superior load bearing is needed, in contrast to other options, such as HIP. This has also been attempted on other metallic materials [29–31]. This is particularly convenient in multifunctional part production. As a matter of fact, an advantage of AM is the possibility of integrating several parts in a single one. In that case, FSP can be applied in the regions that will be subjected to significant mechanical stresses, i.e. regions of stress concentration. Furthermore, taking into account the necessity of a surface finishing step to ensure good fatigue resistance, FSP can be very adequately implemented, since it can be performed in the same machining centre in what could be considered a single post-processing step.

A more precise example of application of FSP in AM can be low tolerance holes for part attachment (see Fig. 1). To achieve the accuracy these features require, machining can be needed. In this case, the use of FSP would be possible and recommended. The following sequence would be applied: FSP to obtain a zone with good mechanical behaviour; machining of the hole in this zone; surface finishing. This would result in a zone surrounding the hole that will experience significant mechanical load, but will bear it thanks to the improvement provided by the FSP and the good surface quality. The intended enhancement is therefore in the frame of fatigue or cyclic loading.

There is a significant number of fatigue studies on LPBF AlSi10Mg [5], with however limited success in the way of fatigue life improvement. It is often the case that the presence of notably large pores, of equivalent diameter attaining ranges of hundreds of microns [32–34], drastically affects fatigue behaviour, compromising the analysis and the applicability of eventual conclusions to other examples not presenting such a high level of defects. Note that porosity smaller than 50 μm in equivalent diameter can already have a critical influence on fatigue crack nucleation, jeopardising fatigue life [7].

Larrosa et al. [14] achieved up to 65 % porosity reduction by HIP preceded by T6 treatment, but neither this nor the T6 treatment alone, which even increased porosity slightly, managed to improve fatigue life. Schneller et al. [22] obtained no enhancement after SRHT and only a modest 21% improvement with HIP, in contrast to the 374% and 74% increase in fatigue strength for HIP post-treated Scalmalloy and 17.4PH steel, respectively. The HIP post-processing did not reduce void expansion in LPBF AlSi10Mg as significantly as in the other two materials (−13%, −92% and −96%, respectively). Uzan et al. [24] even reported a reduction of fatigue life after HIP and attributed it to the marked microstructure coarsening and thus significant strength loss. A potential solution to this deleterious effect of HIP could be a subsequent heat treatment, but, besides the issue of increased post-processing complexity, it can

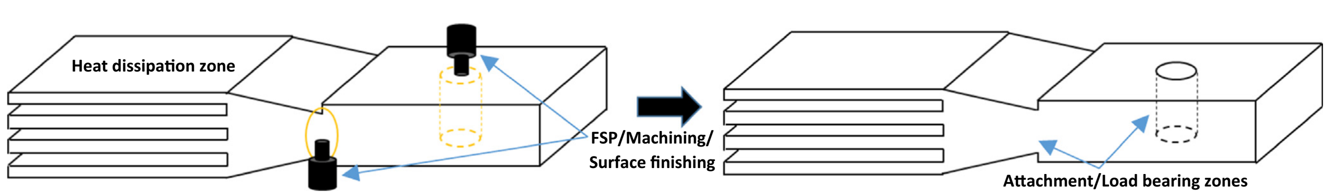

Fig. 1. Figurative additive manufactured multifunctional part that can be enhanced by post-treatment. The left zone has a heat dissipation role while the central and right zones are subjected to mechanical loads. Zones of stress concentration (in orange) can be friction stir processed to obtain superior mechanical properties locally. (For interpretation of the references to colour in this figure legend, the reader is referred to the web version of this article.)

also bring about pore reopening due to the inefficient sealing effect of the HIP treatment (observed both in LPBF AlSi10Mg [35] and Ti6Al4V [36] and electron beam melting Ti6Al4V [37]), further justifying the pertinence of the search for alternatives.

Studies on cyclic behaviour of LPBF AlSi10Mg have been aimed at total fatigue life, without distinguishing between crack nucleation and growth. Limited research on the latter aspect has been performed [17,38,39]. Di Giovanni et al. [17] indeed focused on fatigue crack growth (FCG), which they found to be facilitated by the presence of the Si-rich interconnected network in the AB material. This network was concluded to offer an easier propagation path. An influence of the melt pool mesostructure was also observed. A decrease of the FCG rate was achieved thanks to the elimination of these two detrimental features after a T6 treatment and its globularisation and homogenisation effects [17]. Xu et al. [39] reported better fatigue resistance when the direction of crack growth is along (or differing 15° from) the build platform direction and linked fatigue crack propagation differences to the presence and orientation of the melt pool border.

In this work the fatigue of LPBF AlSi10Mg is studied. Constant amplitude S-N and crack growth curves have been obtained. A comparison between the AB and post-processed states (SRHT and FSP) allows to elucidate the different factors (porosity, microstructure) influencing fatigue life. Both post-treatments reduce fatigue crack growth by an order of magnitude, presumably due to the more important plasticity induced crack closure and crack branching phenomena. FSP produces a very significant porosity reduction effect in an efficient and reliable way that other techniques, such as HIP, fail to achieve. This results in crack nucleation delay and total fatigue life improvement even above ten times.

2. Experimental methods

The initial additive manufactured material, in the form of 150 × 35 × 5 mm plates, was produced with an EOS M290 laser powder bed fusion machine, using AlSi10Mg aluminium alloy powder. The following manufacturing parameters were used: Power = 370 W; laser advance speed = 1300 mm/s; layer thickness = 30 μm; hatch spacing = 0.19 mm; rotation angle between layers = 67°. These parameters were priorly optimised by the machine manufacturer for the AlSi10Mg alloy [18].

Post-processing performed on the LPBF material consisted in either SRHT at 300 °C during 2 h under argon atmosphere and furnace cooling or FSP. The latter was performed on a Hermle UWF 1001H milling machine using an H13 steel tool with a 20 mm diameter scrolled shoulder, a 4.6 mm long and 6 mm diameter threaded triflute pin [40], a tilt angle of 1°, a rotation speed of 1000 rpm and an advancing speed of 500 mm/min or 1000 mm/min.

Samples were extracted from said plates before and after post-treatment for microstructural characterisation. To perform scanning electron microscopy (SEM) the surface of the specimens was finely polished and etched with HF 0.5 vol% solution.

To determine the static behaviour of LPBF AlSi10Mg under the four studied conditions, tensile testing was done on round samples conforming to ASTM E8/E8M – 15a standard (see Fig. 2 for geometry reference), with a loading speed of 1 mm/min.

Constant amplitude uniaxial tensile (R = 0.1) fatigue tests were performed following ASTM E466 – 15 standard, on a 10 kN load cell Instron ElectroPuls E10000 test instrument, with a frequency of 30 Hz. Since the aim was to characterise the material properties, small round specimens (Fig. 2) were machined from the LPBF plates, thus decreasing the residual stress level and its possible influence. With the same intention, the samples were mechanically polished down to a $R_a \simeq 0.1$ μm, hence avoiding the surface roughness influence on fatigue life. The sample geometry was already validated in preliminary experiments [7]. Tests were stopped if failure had not occurred after $2{\cdot}10^6$ cycles.

FCG testing was performed on 3.5 mm thick compact tension (CT) samples following ASTM E399 – $12^{\varepsilon3}$, E561 – 15a and E647 – 15 standards, on a 25 kN MTS Bionix servohydraulic test system, also with R = 0.1 and f = 30 Hz. 1 mm pre-cracking was made under a maximum force of 800 N and camera monitoring. The force was reduced to 600 N for the actual FCG testing. The orientation of the FSP specimens can be observed in Fig. 2, the AB and SRHT having an orientation differing 90° with respect to the pictured FSP orientation to study the supposed more favourable case (i.e. crack propagating in the building direction (the z axis)) [17,39]. The two surfaces of the samples were finely polished to avoid the effect of roughness on fatigue behaviour. A clip-on extensometer was used to periodically acquire the extensions at maximum and minimum forces during the experiment. The side surface of the CT FCG specimens was also monitored during the test with a camera equipped with a VS Technology VS-TCH6-65 lens, allowing tracking the crack and measuring its growth. The experiment was divided into the following two steps: A precrack of 1 mm length was obtained through cyclic loading, pausing the loading at intervals to check the precrack length; then, maximum and minimum forces of 600 N and 60 N were applied during the subsequent crack growth test.

Microscopy characterisation was carried out on fatigue samples after failure to further study the fatigue mechanisms of LPBF AlSi10Mg in the different conditions.

3. Results

3.1. Microstructure: Si-rich eutectic phase

The microstructure for the four studied conditions can be observed in Fig. 3. The AB material presents a fine Si-rich eutectic phase forming a network surrounding the α-Al cells (see Fig. 3a). The detail of Fig. 3a shows the fine Si precipitates that are found inside the α-Al cells. A comprehensive analysis of the connectivity of the microstructure of these same samples can be found in Santos Macías et al. [41]. In the same paper, the 3D structure of the Si-rich eutectic network in the coarse melt pool and heat affected zones has been detailed.

Both SRHT and FSP post-processing produce a breakdown and globularisation of the Si-rich network, as can be appreciated in Fig. 3b-d. Some coarsening occurs (more significant in the FSP case) in the Si-rich phase and in the Si precipitates, but a good fineness level is preserved, especially in comparison to T6 or HIP post-treatments [14]. A detailed study of the microstructure and damage mechanisms of the SRHT and FSP at 500 mm/min states compared to the AB condition can be found in Zhao et al. [28]. The microstructure after FSP is finer for the 1000 mm/min tool advancing speed case compared to the 500 mm/min one.

3.2. Tensile properties

The true stress - strain curves for the four different states are depicted in Fig. 4. The high strength of the AB material imparted by its very fine microstructure is decreased due to microstructure coarsening after the post-treatment. The Si-rich network contributes to the strength of the AB LPBF AlSi10Mg with its load bearing capacity [42], but it is also a favourable site for early crack nucleation and propagation, limiting ductility [28]. The breakdown and globularisation of this phase after post–processing effectively eliminate the easy coalescence path, allowing the more ductile α-Al matrix to govern the material behaviour, leading to a very sig-

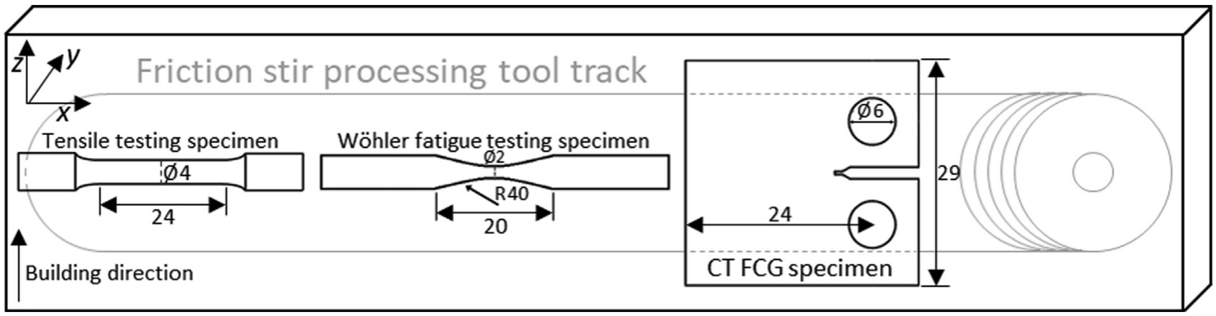

Fig. 2. LPBF AlSi10Mg plates and geometry of the mechanical testing samples. The gray lines represent the FSP trace.

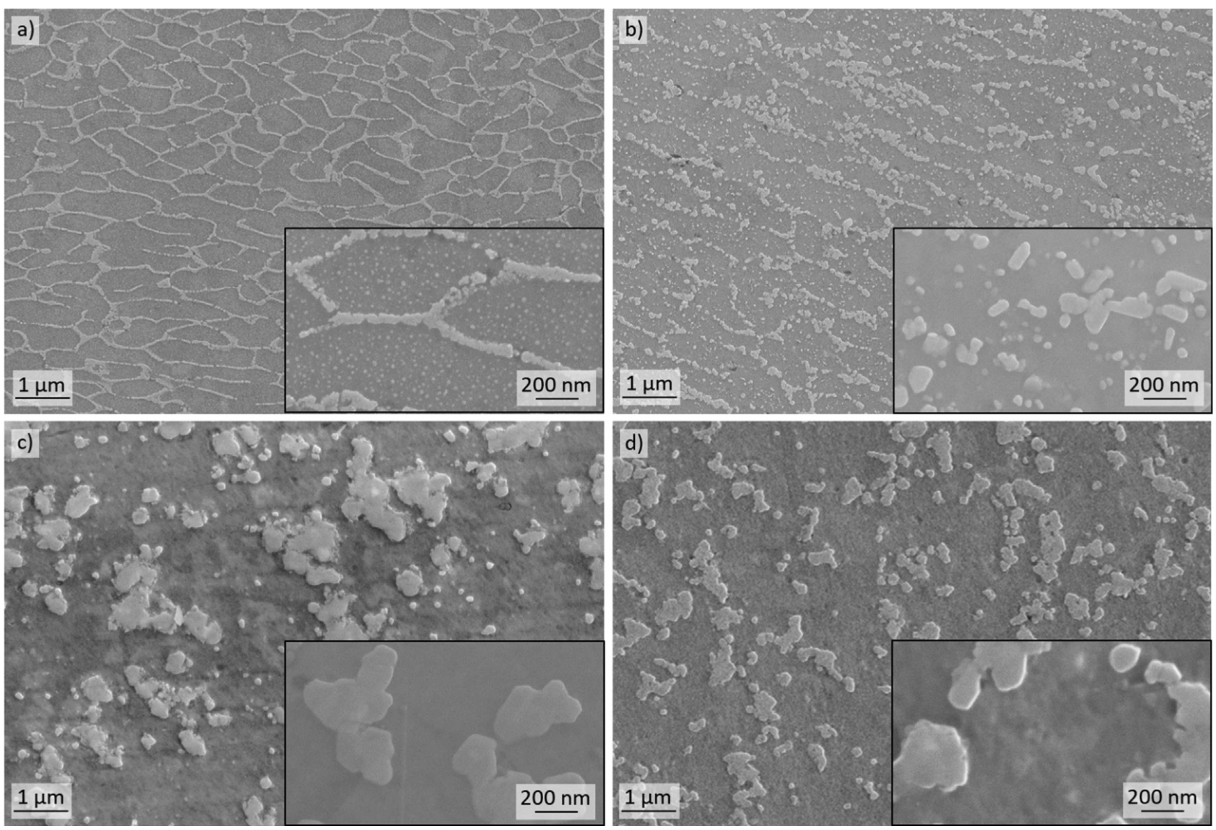

Fig. 3. SEM micrographs of LPBF AlSi10Mg in AB (a), SRHT at 300 °C for 2 h (b), FSP at 500 mm/min (c) and FSP at 1000 mm/min (d) states.

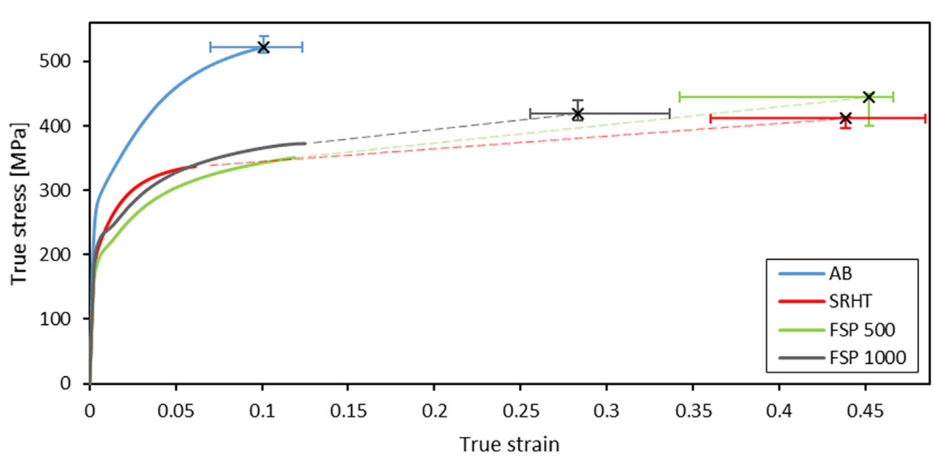

Fig. 4. Tensile curves for LPBF AlSi10Mg under AB, SRHT at 300 °C for 2 h and FSP at 500 mm/min and 1000 mm/min conditions. The bars represent the 99% confidence intervals.

nificant increase in ductility, as discussed and demonstrated by Zhao et al. [28]. The differences between the FSP performed at 500 mm/min and 1000 mm/min can be linked to the Si-rich particle size and distribution. The latter presents smaller particles, hence the higher mechanical strength, but less separated, thus leading to earlier damage coalescence and lower ductility.

3.3. Wöhler fatigue curves and fractography

The Wöhler curves are presented in Fig. 5. The straight lines correspond to the Basquin's fitting law

$$\Delta\sigma = C \cdot N_f^b \tag{1}$$

where $\Delta\sigma = \sigma_{\max} - \sigma_{\min}$, N_f = Number of cycles to failure and b and C [MPa] are material constants, provided in Table 1.

The SRHT does not result in a significant change in total fatigue life of the LPBF AlSi10Mg material. Contrastingly, FSP brings a very significant enhancement. Furthermore, the two different FSP parameter sets seem to yield a very similar behaviour, which highlights the robustness of the process, since a significant variation of parameters would not compromise the total fatigue life improvement as long as they lead to a defect-free material. The strength difference between FSP at 500 mm/min and at 1000 mm/min is therefore limited enough to have a notable impact on fatigue performance, so only the former was further analysed. In this case, only a limited number of Wöhler curve points (four data points) were obtained for the FSP at 1000 mm/min condition since the similarity with FSP at 500 mm/min was clearly very high and a comparison between the various states (AB, SRHT and FSP) is already feasible. Undoubtedly, from an industrial point of view more data points would be needed, but that is not the aim of this work, although it is pertinent in future research, as is the analysis of FSP parameter effect.

Fracture surfaces of fatigue samples tested to obtain the Wöhler curves were observed using SEM. In all cases the crack responsible for failure initiated from the surface. In the AB and SRHT specimens relatively large ($Ø_{eq} \simeq 50\ \mu m$) lack of fusion defects could clearly be identified as the cause of crack initiation (see Fig. 6a,b). In the FSP samples no clear defect could be identified (Fig. 6c).

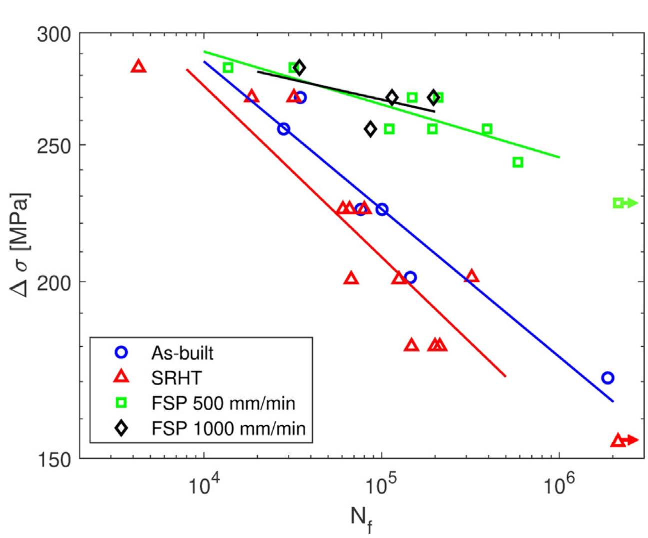

Fig. 5. Wöhler curves for LPBF AlSi10Mg AB, SRHT at 300 °C for 2 h and FSP at 500 mm/min and 1000 mm/min states. The straight lines correspond to Basquin's law fitting of the data from failed samples. The arrowed points represent run-outs.

3.4. Fatigue crack growth and fracture path observations

Taking into account the similar fatigue resistance of the material after FSP at 500 mm/min or at 1000 mm/min, only the former was used for further fatigue experiments. CT FCG testing was therefore performed on LPBF AlSi10Mg AB, SRHT and FSP at 500 mm/min samples. Two tests per condition were performed, with a satisfactory reproducibility, as can be appreciated in Figs. 7 and 8, which respectively depict the crack length growth curves derived from clip-on extensometer reading and camera imaging and the FCG rate curves obtained from treatment of the clip-on extensometer data. For the AB condition, the crack propagation direction for the AB I specimen was from the top to the bottom of the plate it was machined from (along the negative z axis direction in Fig. 2), and the opposite for the AB II sample (i.e. following the building direction). No significant difference is found between these two AB specimens. For the SRHT samples, the sense was the same as for AB I.

The CT FCG testing allows to measure the crack length during its propagation (see Fig. 7). This was done in two ways, with the clip-on extensometer and with the side camera imaging of the surface crack, obtaining a good correlation between the two methods. A difference of an order of magnitude can be appreciated in fatigue life before and after post-treatment, with the FSP material presenting the highest number of cycles to failure.

The straight lines in Fig. 8 represent the Paris' law fitting of the data

$$\frac{da}{dN} = A(\Delta K)^m \tag{2}$$

where nominal values (i.e. not corrected for closure) of ΔK have been used. The values for A and m are given in Table 2. The A and m parameters are within an expected range for LPBF AlSi10Mg, see Di Giovanni et al. [17]. It is important to note that the condition for linear elastic fracture mechanics (LEFM, ASTM E647 – 15 standard) is verified everywhere for the as built material and only for ΔK < 15-MPa·m$^{1/2}$ for the SRHT and FSP samples. The LEFM invalid region is not part of the Paris regime (see Fig. 8) and is thus not affecting the results in Table 2. However, in that region the calculation of ΔK should be considered invalid.

The fatigue crack growth rate is reduced by an order of magnitude through post-processing, be it SRHT or FSP. At the beginning of crack propagation the FSP material presents a slightly lower crack growth rate than the SRHT. Since the crack propagation acceleration is slightly higher for the FSP specimens, the rate eventually becomes a bit higher for the FSP in comparison to the SRHT at the end part of the stable crack growth stage.

The camera imaging also allows to characterise the fatigue crack behaviour at a mesoscopic scale. Surfaces of CT FCG samples showing the advancing crack are pictured in Fig. 9. Two parallel yellow lines spaced 100 μm help to visualise and compare crack deviation. The melt pool structures present in the AB and SRHT conditions are visible in Fig. 9a,b. The fatigue crack is very slightly deviated by the melt pool borders in the AB and SRHT states (Fig. 9a,b). Such deviation does not occur after FSP, since its homogenisation effect eliminates the melt pool structure (see Fig. 9c).

Microscopy characterisation of the CT FCG samples crack area was performed to elucidate the crack path in relation to the microstructure. The crack zone corresponding to a ΔK level around 9 MPa·m$^{1/2}$ (Paris regime) can be observed in Fig. 10a-c. The post-processed materials present a rougher crack path and more branching cracks. Examples of these secondary cracks can be observed in more detail in Fig. 10d-f. They vary in length, being around 1 μm for the AB samples, a few microns in the FSP case and reaching several microns in the SRHT condition. Slight damage

Table 1
Parameters of Basquin's law.

Parameters of Basquin's law	AB	SRHT	FSP 500	FSP 1000
C [MPa]	750	840	411	373
b	−0.1	−0.12	−0.04	−0.03

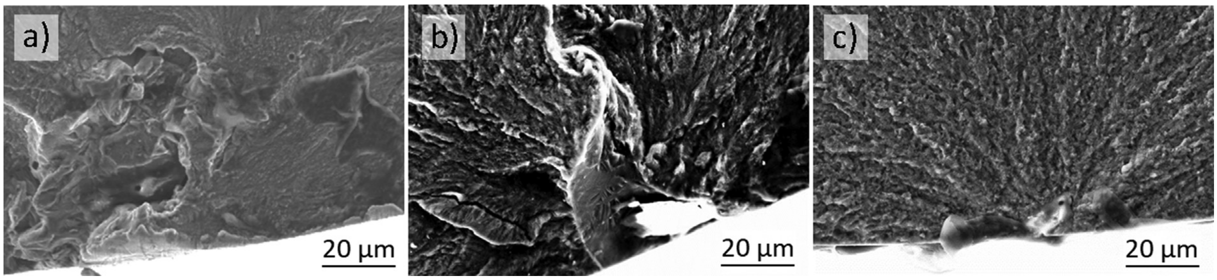

Fig. 6. SEM fractography micrographs of the fatigue crack nucleation sites for LPBF AlSi10Mg under AB (a), SRHT at 300 °C for 2 h (b) and FSP at 1000 rpm and 500 mm/min (c) conditions.

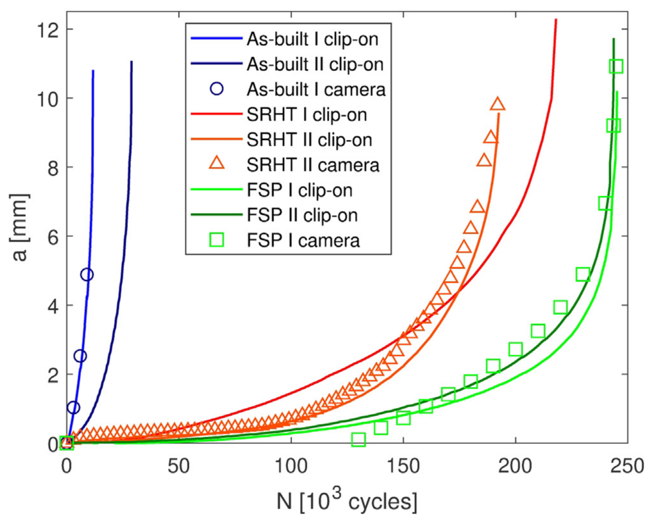

Fig. 7. FCG for LPBF AlSi10Mg under AB, SRHT at 300 °C for 2 h and FSP at 500 mm/min conditions. The continuous curves are derived from clip-on extensometer data and the dotted ones from crack imaging.

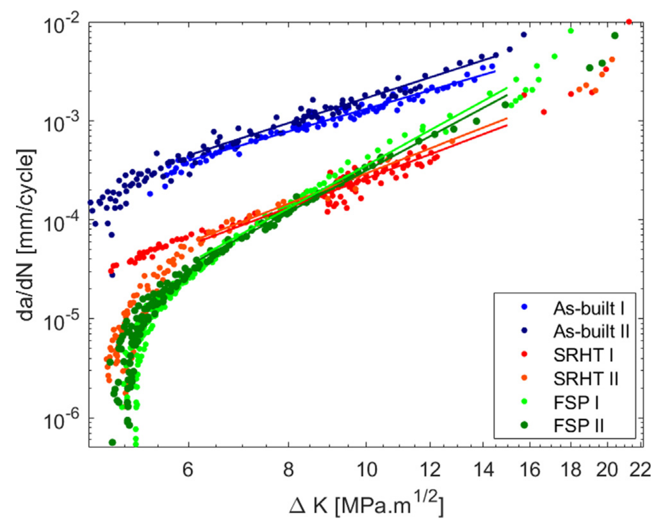

Fig. 8. FCG rate curves for LPBF AlSi10Mg in AB, SRHT at 300 °C for 2 h and FSP at 500 mm/min states. The straight lines correspond to the linear part of the curve and were obtained applying a Paris' law fitting to the data.

nucleation at the AB Si-rich network can be appreciated at the vicinity of the crack in Fig. 10d. Damage nucleation on Si-rich particles and decohesion of Si-rich particles and α-Al matrix events can be observed in Fig. 10f, indicating that damage in the post-treated specimens is more significant.

4. Discussion

4.1. Fatigue crack nucleation

The AB LPBF AlSi10Mg material has a very good strength to weight ratio, but the presence of porosity (see Fig. 6a) leads to early fatigue crack nucleation, with a consequent limited fatigue resistance. This porosity is inherent to the LPBF process, stemming from lack of fusion or trapped gas during manufacturing [7,9,10,15,19]. The changes produced by an SRHT do not have a very significant impact on fatigue, since the main culprit of the poor cyclic performance, porosity (see Fig. 6b), is not affected. Indeed, the very similar porosity level of AB and SRHT samples has been determined by X-ray tomography analysis to be around 0.13% by Santos Macías et al. [7] for samples with exactly the same process parameters.

Higher stress concentration factor at surface or subsurface level leads to fatigue crack nucleation in defects found in this superficial region [43,44]. For good fatigue resistance it is thus essential to achieve a superficial volume free of defects. In this sense, a good surface roughness level can be obtained by surface finishing. However, the issue of superficial region porosity remains. A possible solution is the FSP post-treatment.

FSP produces a very significant improvement in fatigue resistance of LPBF AlSi10Mg (see Fig. 5). The very notable enhancement has to be mainly linked to the porosity reduction effect of this post-treatment. In fact, the porosity level is around 0.03% after FSP, and, perhaps more importantly for fatigue crack nucleation, the volume fraction of porosity of equivalent diameter above 5 μm decreases from 0.09% for AB and SRHT to 0.02% for FSP, and the maximum pore size from 50 μm to 10 μm [7]. Furthermore, other changes, such as the microstructural globularisation, are also occurring with SRHT, impacting strength and ductility, but without improving fatigue life as it occurs with FSP [24]. Indeed, the very slight decrease in fatigue resistance from the AB to the SRHT state could be due to the lower yield strength.

Table 2
Parameters of Paris' law.

Parameters of Paris' law	AB		SRHT		FSP 500	
	I	II	I	II	I	II
A	5.8x10^{-6}	4.2x10^{-6}	2.3x10^{-7}	2.1x10^{-7}	1.2x10^{-8}	1.5x10^{-8}
m	2.4	2.6	3.1	3.2	4.5	4.3

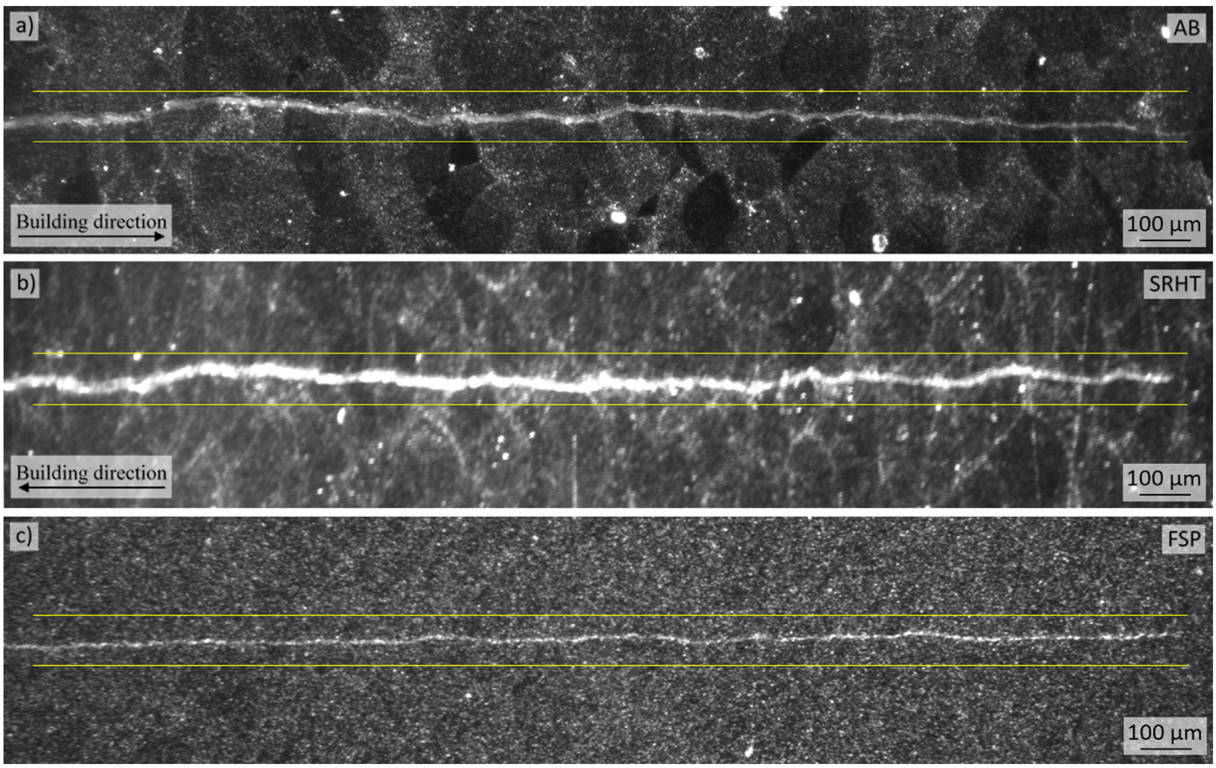

Fig. 9. CT FCG specimen surface for LPBF AlSi10Mg under AB (a), SRHT at 300 °C for 2 h (b) and FSP at 500 mm/min (c) conditions. Yellow parallel lines spaced 100 μm serve to apprehend and compare crack deviation. (For interpretation of the references to colour in this figure legend, the reader is referred to the web version of this article.)

The effect of FSP post-treatment on the S-N curves seems to be more important at low stress levels. One reason for this could be that at relatively high stress levels damage in the FSP specimens could act as fatigue crack nucleation sites, playing a similar role to the initial porosity in AB or SRHT samples. Indeed, this phenomenon does not have such a significant impact on the AB and SRHT specimens because they already present critically large porosity acting as fatigue crack nucleation sites. In the FSP case, the largest Si-rich eutectic phase particles [7,28] or even large Fe-rich intermetallics can fracture and nucleate damage under high stress levels. Moreover, damage nucleation occurs at an earlier stage in the FSP samples compared to the SRHT specimens since they present larger Si-rich particle size [28]. Lower $\Delta\sigma$ does not lead to such critical damage on the FSP material that would act as fatigue crack nucleation sites.

The two different FSP conditions, 500 mm/min and 1000 mm/min tool advance speed, allow to establish FSP as a robust and flexible solution for fatigue resistance enhancement. Moreover, it is interesting to see that the differences in static mechanical properties for the two FSP conditions patent in Fig. 4 do not seem to have an impact on fatigue. This could mean that porosity and the fatigue crack nucleation stage are more influential on the overall fatigue life than the strength or ductility differences between the two FSP conditions.

The fractography analysis of S-N samples reveals that cracks leading to failure initiate from lack of fusion defects located at the surface (see Fig. 6a,b). The FSP specimens do not show a clear defect leading to fatigue crack nucleation (see Fig. 6c). After FSP, the large porosity is eliminated, removing the critical fatigue crack nucleation cause. Thus, the onset of fatigue in the FSP material could stem from oxides, Si-rich particles or Fe-rich intermetallics, features that had a secondary relevance in the AB and SRHT samples, overshadowed by the large porosity. This confirms the importance of large porosity (i.e. $Ø_{eq}$ > 10 μm) elimination for fatigue life improvement [7].

4.2. Fatigue crack growth

The second main aspect of fatigue life is the fatigue crack propagation. The CT FCG testing shows that both post-treatments significantly reduce the growth rate compared to the AB condition (see Fig. 8). The slope of the Paris curve is however slightly higher for the FSP condition compared to the SRHT.

Fatigue crack growth is a very complex and multimodal phenomenon. It can be influenced by varied aspects such as cyclic strain hardening, presence of oxides or residual stress fields [45–49]. In the case at hand one factor that could account for the improvement of FCG after post-processing could be plasticity induced crack closure [45–47]. Looking at Fig. 4 it can be concluded that for the post-treated materials, having a lower yield strength, the size of the crack tip plastic zone will be larger for a given ΔK value and crack closure should be more pronounced. This could account for the slower fatigue crack growth of the SRHT and FSP materials observed in Fig. 8 (nominal values for ΔK). A finite ele-

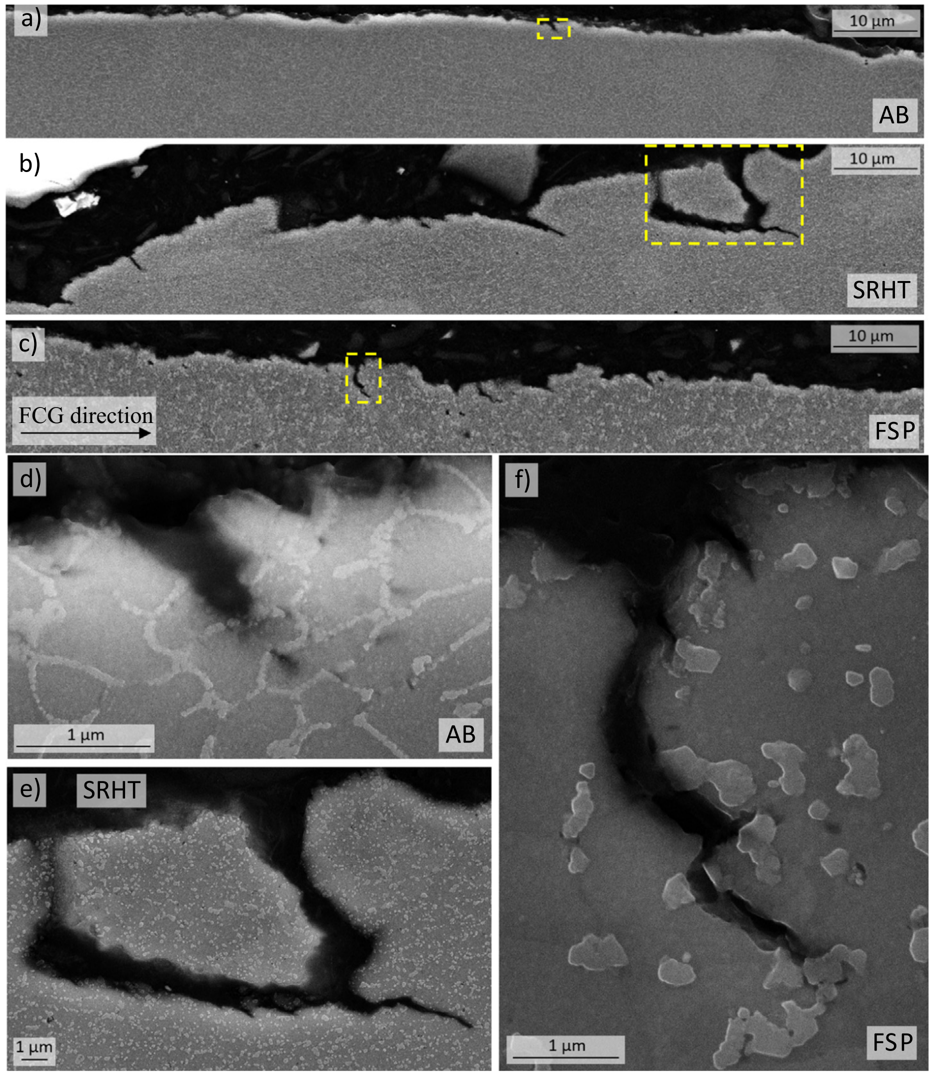

Fig. 10. SEM micrographs of the crack zone of CT FCG samples of LPBF AlSi10Mg in AB (a,d), SRHT at 300 °C for 2 h (b,e) and FSP at 500 mm/min (c,f) states.

ment simulation of the CT FCG specimens (see supplementary material section) confirms that the plastic zone in front of the crack tip is smaller in the AB sample. The SRHT and FSP plastic zones are much larger, the latter extending the furthest.

At a mesoscopic (i.e. melt pool level) scale the AB and SRHT CT FCG specimens present slight crack deviation due to the presence of the melt pool structure (see Fig. 9 and the videos provided as supplementary material). This structure and its modest effect on crack path are eliminated after FSP. This may explain the higher slope m for the FSP case. The intermediate m value of the SRHT condition could be explained by the fact that the melt pool structure is still present, but, due to a homogenisation effect, the differences between the regions (i.e. melt pool border and rest of the melt pool) are not as marked as for the AB state. The melt pool border is constituted of the coarse melt pool (CMP) and heat affected zones. The former is similar to the fine melt pool (FMP) zone of the rest of the melt pool, but has a slightly coarser microstructure [28]. This means, as discussed by Zhao et al. [50], that the strength of the CMP is lower than that of the FMP and the crack will thus progress with more ease through the melt pool border, which explains why it slightly deviates towards and follows it. Note the possible importance of the orientation of the FCG samples. In the studied case, i.e. propagation along the building direction, the melt pools are oriented in such a way that their borders promote crack deflection and can have a toughening effect. If the propagation was perpendicular to the building direction, then the melt pool borders could act as paths promoting an uninterrupted easier crack advance as discussed by Di Giovanni et al. [17], who observed faster crack propagation in the direction perpendicular to the building direction. Furthermore, the crack growth sense does not seem to have a significant influence on the results for the AB specimens (that is, at least in the build direction plane). In AB I the crack propagates downwards, towards the build platform end, whereas in AB II the sense is upwards. This observation is also in agreement with the conclusions of Di Giovanni et al. [17].

At a more microscopic scale, the crack path shows much more crack branching for the post-treated samples (see Fig. 10a-c). On the contrary, events of secondary cracking are scarce in the AB specimens and their size is also very limited, not exceeding 1 µm (see Fig. 10a,d). This is due to the high strength of the AB material, which reduces damage in the surroundings of the crack. This is coupled with the presence of the Si-rich network, which, being more brittle than the α-Al matrix, drives the advance of the fatigue crack, be it through damage nucleation in the network or through decohesion of the Si-rich/α-Al phases interface.

The post-processed materials present more branching cracks that consume energy and delay the fatigue crack growth (see Fig. 10b,c) [46]. These secondary cracks are also of a larger size.

The post–treated materials have lower strength, allowing for more damage in the form of crack nucleation in particles and particle/-matrix decohesion, as can be appreciated in Fig. 10f. Comparing the two post-treatments, the FSP branching cracks are shorter. This could stem from the difference in damage nature of the SRHT and FSP materials, which was studied by Zhao et al. [28]. The former presents smaller but more numerous damage events at a smaller distance from each other. The latter, with bigger particles that are more spaced out, presents larger damage events, which could mean more energy dissipation and lower fatigue crack growth. These nucleated cavities are however at a larger distance from each other. Secondary cracks seem to grow more in the SRHT specimen, where the distance between damage events is smaller.

Other mechanisms, such as the aforementioned cyclic strain hardening, could play a role in fatigue crack growth. Significant strain hardening can contribute to crack closure [48,49]. However, in the present case no conclusions can be drawn on the effect of this aspect due to the lack of cyclic data. The same goes for other phenomena, like residual stress fields, which can be present in the studied material and in AM parts in general [51], but will be significantly modified and reduced in the preparation and machining of the fatigue testing specimens.

Comparing the FSP and SRHT conditions, the slope is different in Fig. 8, the FSP curve is stiffer (hence lower propagation speed at the beginning and higher at the end). In the FSP samples crack initiation occurs later, and initially crack growth is slower. Some of the reasons for the difference of crack growth nature in the FSP state could be the following:

- Absence of melt pool border and its possible crack growth rate delaying effect, hence the higher acceleration in the FSP case
- Absence of critical large porosity [7], which delays early stage crack growth. The presence of porosity could have a more significant impact at the beginning of crack growth since these defects, of significantly larger size than the Si-rich eutectic phase, could be more sensitive to the initial and relatively low stress concentration.
- Presence of larger size Si-rich eutectic phase in the FSP material [28]. At an early stage, it is smaller than the porosity defects, but as the crack and the stress intensity grow, this phase (smaller for the AB and SRHT cases) will have an increasing impact, eventually leading to crack growth acceleration.

It should be noted that, especially in the presence of significant porosity, which is the case of AB and SRHT states, the essential part of fatigue life is dictated by fatigue crack nucleation. Fatigue crack growth only accounts for a small fraction of total life. Thus, even if fatigue crack growth is slower for the SRHT case, its impact on total life is quite limited. Furthermore, yield and ultimate tensile strength are lower for the SRHT material compared to the AB. This could have an effect on nucleation, since the material surrounding a defect or porosity would undergo larger plastic deformation and thus lead to the critical fatigue crack earlier. In the FSP case, the improvement of fatigue crack growth rate, combined with the smaller initial defect size, will lead to more propagation cycles. On the other hand, the nucleation stage will also be longer, due to smaller initial defect size, and, probably, proportionally more so.

5. Conclusion

The fatigue properties of LPBF AlSi10Mg in AB, SRHT and FSP states have been studied. The following main points can be highlighted as findings of this research:

- In AB and SRHT conditions fatigue cracks initiate from lack of fusion defects. The SRHT treatment has no positive effect on the total fatigue life of the material.
- The reduction of porosity and the elimination of the larger pores through the FSP post-treatment, achieved with two different tool advance speeds, leads to a very significant improvement of total fatigue life. FSP is especially flexible and adequate to treat parts locally, only in the zones where specific mechanical behaviour is needed, i.e. typically in regions of stress concentration. FSP can be implemented in the surface finishing step, in contrast to the HIP alternative, which is besides still to be proven as a viable solution for AM Al alloys.
- The fatigue crack growth rate is decreased by an order of magnitude after SRHT or FSP. The following three possible reasons have been proposed:
  - i) Increased plasticity induced crack closure for the SRHT and FSP materials compared to AB reducing the SRHT and FSP crack growth rate.
  - ii) Very slight crack deviation by the melt pool borders in the AB and SRHT samples, which would be in favour of a slower crack growth rate in the SRHT and AB materials, but its magnitude seems limited. This could however partially explain the slightly lower Paris law exponent of the SRHT sample compared to FSP.
  - iii) Increased crack branching in the FSP and SRHT samples reducing the SRHT and FSP crack growth rate. This phenomenon seems more important in the SRHT material than in the FSP condition and could contribute to the Paris law exponent difference more notably than the previous reason.

FSP can be postulated as a very robust and flexible solution to improve fatigue resistance thanks to its porosity reduction effect, with a certain tailorability of static mechanical properties.

Declaration of Competing Interest

The authors declare that they have no known competing financial interests or personal relationships that could have appeared to influence the work reported in this paper.

Acknowledgements

The authors acknowledge the support of Laurence Ryelandt (UCLouvain). JGSM acknowledges the support of the Fonds de la recherche scientifique - FNRS (FRIA grant), Belgium. This research has also been funded (from January 2017) by the European Research Council (ERC) under the European Union's Horizon 2020 research and innovation program (grant agreement n °716678). This research work has also been supported from January 2019 by the WALInnov LongLifeAM project, Convention n °1810016, funded by the Service public de Wallonie Économie Emploi Recherche (SPW-EER). Published with the support of the Fondation Universitaire de Belgique.

Data availability

The authors confirm that their data are available.

Appendix A. Supplementary material

Supplementary data to this article can be found online at https://doi.org/10.1016/j.matdes.2021.110084.

References

[1] S. Nishida, Failure analysis in engineering applications, first ed., Butterworth Heinemann, Oxford, 1992.
[2] Z. Tang, H. Jing, L. Xu, L. Zhao, Y. Han, H. Li, N. Ma, Investigation of creep-fatigue crack growth of G115 steel using a novel damage model, Int. J. Mech. Sci. 183 (2020) 105827.
[3] D. Lin, L. Xu, H. Jing, Y. Han, L. Zhao, Y. Zhang, H. Li, A strong, ductile, high-entropy FeCoCrNi alloy with fine grains fabricated via additive manufacturing and a single cold deformation and annealing cycle, Addit. Manuf. 36 (2020) 101591.
[4] C. Gosselin, R. Duballet, P. Roux, N. Gaudillière, J. Dirrenberger, P. Morel, Large-scale 3D printing of ultra-high performance concrete - a new processing route for architects and builders, Mater. Des. 100 (2016) 102–109.
[5] N.T. Aboulkhair, M. Simonelli, L. Parry, I. Ashcroft, C. Tuck, R. Hague, 3D printing of aluminium alloys: additive manufacturing of aluminium alloys using selective laser melting, Prog. Mater. Sci. 106 (2019) 100578.
[6] Q. Yan, B. Song, Y. Shi, Comparative study of performance comparison of AlSi10Mg alloy prepared by selective laser melting and casting, J. Mater. Sci. Technol. 41 (2020) 199–208.
[7] J.G. Santos Macías, C. Elangeswaran, L. Zhao, B. Van Hooreweder, J. Adrien, E. Maire, J.Y. Buffière, W. Ludwig, P.J. Jacques, A. Simar, Ductilisation and fatigue life enhancement of selective laser melted AlSi0Mg by friction stir processing, Scr. Mater. 170 (2019) 124–128.
[8] C. Weingarten, D. Buchbinder, N. Pirch, W. Meiners, K. Wissenbach, R. Poprawe, Formation and reduction of hydrogen porosity during selective laser melting of AlSi10Mg, J. Mater. Process. Technol. 221 (2015) 112–120.
[9] M. Tang, P.C. Pistorius, J.L. Beuth, Prediction of lack-of-fusion porosity for powder bed fusion, Addit. Manuf. 14 (2017) 39–48.
[10] N. Sanaei, A. Fatemi, Defects in additive manufactured metals and their effect on fatigue performance: a state-of-the-art review, Prog. Mater. Sci. 117 (2021) 100724.
[11] E. Brandl, U. Heckenberger, V. Holzinger, D. Buchbinder, Additive manufactured AlSi10Mg samples using Selective Laser Melting (SLM): microstructure, high cycle fatigue, and fracture behavior, Mater. Des. 34 (2012) 159–169.
[12] T.M. Mower, M.J. Long, Mechanical behavior of additive manufactured, powder bed laser–fused materials, Mater. Sci. Eng. A 651 (2016) 198–213.
[13] N.T. Aboulkhair, I. Maskery, C. Tuck, I. Ashcroft, N.M. Everitt, Improving the fatigue behavior of a selectively laser melted aluminium alloy: Influence of heat treatment and surface quality, Mater. Des. 104 (2016) 174–182.
[14] N.O. Larrosa, W. Wang, N. Read, M.H. Loretto, C. Evans, J. Carr, U. Tradowsky, M. M. Attallah, P.J. Withers, Linking microstructure and processing defects to mechanical properties of selectively laser melted AlSi10Mg alloy, Theor. Appl. Fract. Mech. 98 (2018) 123–133.
[15] P. Ferro, A. Fabrizi, F. Berto, G. Savio, R. Meneghello, S. Rosso, Defects as a root cause of fatigue weakening of additively manufactured AlSi10Mg components, Theor. Appl. Fract. Mech. 108 (2020) 102611.
[16] Z.M. Jian, G.A. Qian, D.S. Paolino, A. Tridello, F. Berto, Y.S. Hong, Crack initiation behavior and fatigue performance up to very-high-cycle regime of AlSi10Mg fabricated by selective laser melting with two powder sizes, Int. J. Fatigue 143 (2021) 106013.
[17] M.T. Di Giovanni, J.T.O. de Menezes, G. Bolelli, E. Cerri, E.M. Castrodeza, Fatigue crack growth behavior of a selective laser melted AlSi10Mg, Eng. Fract. Mech. 217 (2019) 106564.
[18] E.O.S. GmbH, electro optical systems, Material data sheet for EOS aluminium AlSi10Mg, München (2014).
[19] E.O.S. GmbH, electro optical systems, Material data sheet for EOS aluminium AlSi10Mg, München (2018).
[20] A. du Plessis, S. Beretta, Killer notches: The effect of as-built surface roughness on fatigue failure in AlSi10Mg produced by laser powder bed fusion, Addit. Manuf. 35 (2020) 101424.
[21] S. Beretta, M. Gargourimotlagh, S. Foletti, A. du Plessis, M. Riccio, Fatigue strength assessment of 'as built' AlSi10Mg manufactured by SLM with different build orientations, Int. J. Fatigue 139 (2020) 105737.
[22] W. Schneller, M. Leitner, S. Leuders, J.M. Sprauel, F. Grün, T. Pfeifer, O. Jantschner, Fatigue strength estimation methodology of additively manufactured metallic bulk material, Addit. Manuf. (2020) 101688.
[23] A.H. Maamoun, S.C. Veldhuis, M. Elbestawi, Friction stir processing of AlSi10Mg parts produced by selective laser melting, J. Mater. Process. Technol. 263 (2019) 308–320.
[24] N.E. Uzan, R. Shneck, O. Yeheskel, N. Frage, Fatigue of AlSi10Mg specimens fabricated by additive manufacturing selective laser melting (AM-SLM), Mater. Sci. Eng. A 704 (2017) 229–237.
[25] Y. Wang, J. Shi, Effect of hot isostatic pressing on nanoparticles reinforced AlSi10Mg produced by selective laser melting, Mater. Sci. Eng. A 788 (2020) 139570.
[26] R.S. Mishra, Z.Y. Ma, Friction stir welding and processing, Mater. Sci Eng. R 50 (2005) 1–78.
[27] T. Yang, K. Wang, W. Wang, P. Peng, L. Huang, K. Qiao, Y. Jin, Effect of friction stir processing on microstructure and mechanical properties of AlSi10Mg aluminum alloy produced by selective laser melting, JOM 71 (2019) 1737–1747.
[28] L. Zhao, J.G. Santos Macías, L. Ding, H. Idrissi, A. Simar, Damage mechanisms in selective laser melted AlSi10Mg under as built and different post-treatment conditions, Mater. Sci. Eng. A 764 (2019) 138210.
[29] C. Huang, X. Yan, L. Zhao, M. Liu, W. Ma, W. Wang, J. Soete, A. Simar, Ductilization of selective laser melted Ti6Al4V alloy by friction stir processing, Mater. Sci. Eng. A 755 (2019) 85–96.
[30] P. Peng, K. Wang, W. Wang, P. Han, T. Zhang, Q. Liu, S. Zhang, H. Wang, K. Qiao, J. Liu, Relationship between microstructure and mechanical properties of friction stir processing AISI 316L steel produced by selective laser melting, Mater. Char. 163 (2020) 110283.
[31] Q. Deng, Y. Wu, N. Su, Z. Chang, J. Chen, L. Peng, W. Ding, Influence of friction stir processing and aging heat treatment on microstructure and mechanical properties of selective laser melted Mg-Gd-Zr alloy, Addit. Manuf. 44 (2021) 102036.
[32] S. Romano, S. Beretta, A. Brandão, J. Gumpinger, T. Ghidini, HCF resistance of AlSi10Mg produced by SLM in relation to the presence of defects, Procedia Struct. Integr. 7 (2017) 101–108.
[33] S. Romano, A. Brandão, J. Gumpinger, M. Gschweitl, S. Beretta, Qualification of AM parts: Extreme value statistics applied to tomographic measurements, Mater. Des. 131 (2017) 32–48.
[34] Y. Nadot, C. Nadot-Martin, W.H. Kan, S. Boufadene, M. Foley, J. Cairney, G. Proust, L. Ridosz, Predicting the fatigue life of an AlSi10Mg alloy manufactured via selective laser melting by using data from Computed Tomography, Addit. Manuf. 32 (2019) 100899.
[35] J.C. Hastie, M.E. Kartal, L.N. Carter, M.M. Attallah, D.M. Mulvihill, Classifying shape of internal pores within AlSi10Mg alloy manufactured by laser powder bed fusion using 3D X-ray micro computed tomography: Influence of processing parameters and heat treatment, Mater. Char. 163 (2020) 110225.
[36] T. Kosonen, K. Kakko, N. Raitanen, Evaluation of pore re-opening after HIP in LPBF Ti-6Al-4V, Powder Metall (2021).
[37] S. Tammas-Williams, P.J. Withers, I. Todd, P.B. Prangnell, Porosity regrowth during heat treatment of hot isostatically pressed additively manufactured titanium components, Scr. Mater. 122 (2016) 72–76.
[38] S. Romano, L. Patriarca, S. Foletti, S. Beretta, LCF behaviour and a comprehensive life prediction model for AlSi10Mg obtained by SLM, Int. J. Fatigue 117 (2018) 47–62.
[39] Z. Xu, A. Liu, X. Wang, Fatigue performance and crack propagation behavior of selective laser melted AlSi10Mg in 0°, 15°, 45° and 90° building directions, Mater. Sci. Eng. A 812 (2021) 141141.
[40] C. Jonckheere, B. de Meester, A. Denquin, A. Simar, Torque, temperature and hardening precipitation evolution in dissimilar friction stir welds between 6061–T6 and 2014–T6 aluminum alloys, J. Mater. Process. Technol. 213 (2013) 826–837.
[41] J.G. Santos Macías, T. Douillard, L. Zhao, E. Maire, G. Pyka, A. Simar, Influence on microstructure, strength and ductility of build platform temperature during laser powder bed fusion of AlSi10Mg, Acta Mat. 201 (2020) 231–243.
[42] X.X. Zhang, A. Lutz, H. Andrä, M. Lahres, W.M. Gan, E. Maawad, C. Emmelmann, Evolution of microscopic strains, stresses and dislocation density during in situ tensile loading of additively manufactured AlSi10Mg alloy, Int. J. Plast. 102946 (2021).
[43] Y. Murakami, Metal fatigue: Effects of small defects and nonmetallic inclusions, second ed., Elsevier, Oxford, 2019.
[44] S. Beretta, S. Romano, A comparison of fatigue strength sensitivity to defects for materials manufactured by AM or traditional processes, Int. J. Fatigue 94 (2017) 178–191.
[45] R.O. Ritchie, Mechanisms of fatigue-crack propagation in ductile and brittle solids, Int. J. Fract. 100 (1999) 55–83.
[46] J. Schijve, Fatigue of structures and materials, first ed., Kluwer Academic Publishers, Dordrecht, 2001.
[47] S. Suresh, Fatigue of materials, Cambridge University Press, Cambridge, 1998.
[48] A.T. Kermanidis, A. Tzamtzis, Analytical modeling of fatigue crack propagation based on cyclic hardening and a characteristic damage length, Int. J. Fatigue 141 (2020) 105864.
[49] J. Bao, Z. Wu, S. Wu, P.J. Withers, F. Li, S. Ahmed, A. Benaarbia, W. Sun, Hot dwell-fatigue behaviour of additively manufactured AlSi10Mg alloy: Relaxation, cyclic softening and fracture mechanisms, Int. J. Fatigue 151 (2021) 106408.
[50] L. Zhao, J.G. Santos Macías, T. Douillard, Z. Li, A. Simar, Unveiling damage sites and fracture path in laser powder bed fusion AlSi10Mg: Comparison between horizontal and vertical loading directions, Mater. Sci. Eng. A 807 (2021) 140845.
[51] L. Zhao, J.G. Santos Macías, A. Dolimont, A. Simar, E. Rivière-Lorphèvre, Comparison of residual stresses obtained by the crack compliance method for parts produced by different metal additive manufacturing techniques and after friction stir processing, Addit. Manuf. 36 (2020) 101499.